Graphene origami structures with superflexibility and highly tunable auxeticity

Duc Tam Ho,[1] Sung Youb Kim,[2] and Udo Schwingenschlögl[1,*]
[1]*Physical Science and Engineering Division, King Abdullah University of Science and Technology, Thuwal 23955-6900, Saudi Arabia*
[2]*Department of Mechanical Engineering, Ulsan National Institute of Science and Technology, Ulsan 44919, South Korea*

(Received 18 May 2020; revised 10 October 2020; accepted 26 October 2020; published 11 November 2020)

The two-dimensional structure of graphene makes it difficult to realize flexibility and auxeticity (negative Poisson's ratio) in graphene-based structures. Using molecular dynamics simulations, we demonstrate for graphene origami structures effective tuning of both the flexibility and Poisson's ratio through the geometry, including the potential to combine superflexibility with a highly tunable negative Poisson's ratio in contrast to any existing graphene-based structure. Auxeticity even can be achieved under large applied strain, both tensile and compressive.

DOI: 10.1103/PhysRevB.102.174106

I. INTRODUCTION

Graphene-based structures with superflexibility are used in many applications such as wearable electronics [1], flexible energy storage [2], and strain sensors [3]. Superflexibility in cellular graphene structures, including foams and sponges with low density [4–8], is available only under compression due to the specific geometry of the pores and weak interconnectivity (van der Waals interactions) between graphene sheets [9]. In addition, these cellular graphene structures show extremely low Young's moduli [10] and poor mechanical resilience [11]. On the other hand, graphene kirigami (graphene with a pattern of cuts) can provide superflexibility in the loading direction only under tension [12–14], showing effective compression perpendicular to the loading direction [15].

For stretching in the i direction and lateral response in the j direction, Poisson's ratio is defined as $\nu_{ij} = -\frac{\partial \epsilon_{jj}}{\partial \epsilon_{ii}}$, where ϵ_{ii} and ϵ_{jj} are the strains in the i and j directions, respectively. While most materials have positive Poisson's ratios, i.e., they contract/expand in a lateral direction when they are stretched/compressed, some materials show the opposite behavior (negative Poisson's ratio, auxetic material). Auxeticity leads to excellent mechanical properties such as enhancement of the shear resistance, indentation resistance, and fracture toughness [16]. Auxetic materials can be used in various applications in aerospace [17], textile [18], medical [19], and strain sensor [20] technology. Since the seminal works of Lakes [21] and Wojciechowski [22] more than three decades ago, research in auxeticity has dealt with model materials [23], natural materials [24,25], and metamaterials [26,27]. On the other hand, analogous work for graphene-based structures is rare. Auxeticity can be obtained at very low temperature in graphene kirigami structures [28] and in thin graphene ribbons [29], and at high temperature (above 1500 K) in thermally rippled graphene [30]. At room temperature auxeticity is found in graphene with ripples induced by vacancies (requiring a large vacancy density, e.g., more than 0.5% when the applied strain exceeds 2–3%) [31] and topological defects (requiring ordered defects) [32]. Considering the above limitations, graphene-based structures with superflexibility under both tension and compression, enhanced stiffness and mechanical resilience, and/or tunable and robust auxeticity are still to be developed.

In this paper, we use molecular dynamics (MD) simulations to show that the flexibility, Poisson's ratio, and Young's modulus of a graphene Miura-origami structure (GMS) formed by pattern-based hydrogenation of graphene are highly tunable by controlling the geometry of the GMS. We demonstrate complete structural recovery even after the application of very large tensile and compressive strains, and Young's moduli three orders of magnitude larger than those of most cellular graphene structures with similar supercompressibility. Furthermore, we find negative Poisson's ratios in a wide range from -2.89 to -0.01 at room temperature, which is much wider than reported for any other graphene-based structure, with the auxeticity persistent in an extremely wide range of strains. While auxeticity was proposed previously for Miura-origami structures [33–35], we introduce in the present paper a method to obtain simultaneously superflexibility (under both tension and compression). This unique combination of extraordinary mechanical properties, e.g., can be used to strongly enhance the sensitivity of strain sensors [20].

II. PATTERN-BASED HYDROGENATION AND SIMULATION METHODS

We carry out MD simulations of the formation of GMSs by pattern-based hydrogenation of graphene sheets to evaluate the response under mechanical loading. Figure 1(a) shows schematically the hydrogenation by random distribution of H atoms in predefined areas on top (magenta) and on bottom (cyan) of a graphene sheet. The interaction between the atoms is modeled by the second generation reactive empirical bond order (REBO-II) potential, using the parameters of Ref. [36]. The hydrogenation locally perturbs the planar sp^2 bonding

*udo.schwingenschlogl@kaust.edu.sa

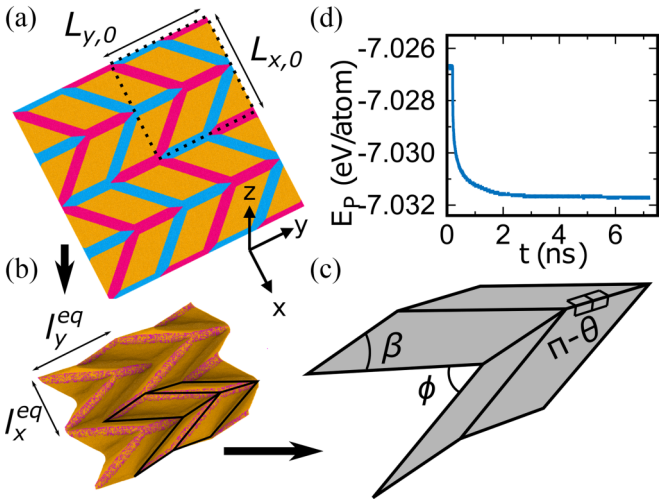

FIG. 1. Schematic of the formation of a GMS by pattern-based hydrogenation of a graphene sheet. (a) Folding pattern showing the areas where the graphene sheet is hydrogenated (magenta, top side; cyan, bottom side). (b) GMS with $L_{x,0} = L_{y,0} = 36.7$ nm, $w = 3.7$ nm, and $\rho = 15\%$ (GMS 1) in the equilibrium state at 300 K. (c) Definition of geometrical parameters. (d) Potential energy of GMS 1 as function of the simulation time at 300 K.

and thus induces pseudo surface stress acting as a driving force to fold the graphene sheet at the hydrogenated areas, resulting in the formation of a GMS. The pattern is characterized by the unit cell dimensions $L_{x,0}$ and $L_{y,0}$, fold width w, and density of hydrogen atoms ρ [ratio of the numbers of hydrogen and carbon atoms in the magenta and cyan areas of Fig. 1(a)]. We apply periodic boundary conditions in the zigzag (x) and armchair (y) directions to eliminate possible edge effects. A 2×2 supercell is considered after confirming that the difference in the obtained structure with respect to a 4×4 supercell is negligible for a GMS with $L_{x,0} = L_{y,0} = 36.7$ nm, $w = 3.7$ nm, and $\rho = 15\%$ (GMS 1).

Initially, a molecular statics simulation is conducted for each GMS (with the supercell dimensions fixed) using the conjugate gradient method with an energy tolerance (relative change of the total energy between successive iterations) of 10^{-16}. The GMS then is relaxed at 300 K under a canonical (NVT) ensemble for 100 ps and afterwards under an isothermal-isobaric (NPT) ensemble (in which the stress components along the in-plane directions are controlled to be zero). According to Fig. 1(d) the relaxation process is well converged. The equilibrium state of GMS 1 is shown in Fig. 1(b). To simulate the mechanical response of a GMS under uniaxial stress in the x direction, starting from the fully relaxed state, the GMS is stretched/compressed in the x direction with a strain rate of $\pm 10^8$ s^{-1} under a NPT ensemble (in which the stress component in the y direction is controlled to be zero). In all MD simulations the temperature and pressure are controlled by a Nosé-Hoover thermostat [37] and barostat [38], respectively, and a time step of 1 fs is chosen. The open-source LAMMPS code [39] is used to perform the molecular statics and MD simulations, and the OVITO software [40] is used to visualize the simulation results.

Our MD simulations for graphene reproduce, applying the same procedure, the low bending stiffness of 0.225 nN nm reported in Ref. [41] (enabling large folding by pseudo surface stress) and are close to the experimental value of 0.192 nN nm derived from the phonon spectrum of graphite [42], implying high predictive power of the implemented simulation approach. In addition, existing experimental techniques [43,44] make it possible to immediately realize the predictions of the present paper: First, hydrogenation with tunable density can be achieved by plasma functionalization [45], thermal cracking [46], and Birch-type hydrogenation [47]. Second, pattern-based hydrogenation of graphene sheets with nanoscale resolution is well established, e.g., 18 nm by electron-beam irradiation [48] and below 10-nm resolution by atomic force microscope lithography [49]. Atomic-scale resolution is accessible by metapromoted hydrogenation [50].

III. RESULTS AND DISCUSSION

The nominal stress component σ_{ij} ($i, j = x, y, z$) is defined as [51]

$$\sigma_{ij} = -\left(\frac{\sum_{k=1}^{N} m_k v_i^k v_j^k}{V} + \frac{\sum_{k=1}^{N'} r_i^k f_j^k}{V} \right), \tag{1}$$

where N is the total number of atoms in the supercell, N' is N plus the number of periodic image atoms outside the supercell, m_k is the mass of atom k, v_i^k is the ith component of the velocity vector of atom k, $V = 4 l_x^{eq} l_y^{eq} h_e$ is the volume [l_x^{eq}/l_y^{eq}, length of the unit cell in the x/y direction in the equilibrium state; h^{eq}, thickness of the GMS (not of graphene) in the equilibrium state], r_i^k is the ith component of the position vector of atom k, and f_i^k is the ith component of the force vector acting on atom k.

Our MD simulation shows that GMS 1 can sustain large compressive strain of at least -85% and large tensile strain of at least 68% without failure [Fig. 2(a)]. We find that σ_{xx} increases slightly in a wide range of ϵ_{xx} [zone 2 of Fig. 2(a)], indicating low in-plane stiffness of GMS 1. In particular, Young's modulus in the x direction (Y_{xx}), which is calculated as the slope of the stress-strain curve in the small strain interval from -1 to 1%, turns out to be 4.6 MPa, which is much smaller than that of pristine graphene (777 GPa, obtained in the strain interval from 0 to 2%). Under the loading the GMS is deformed without significant changes in the atomic distances, while flapping of the graphene pieces connecting at folds [according to Fig. 2(a) the changes of the angles θ and ϕ defined in Fig. 1(c) are large] results in high flexibility and low stiffness. The atomic distances increase significantly when the strain approaches 68% [point B in zone 3 of Fig. 2(a)], where θ becomes zero (flat GMS) according to Fig. 2(b). Similarly, the compressive stress increases significantly when the strain approaches -78% [point A in zone 1 of Fig. 2(a)], where the flapping is largely constrained due to the fact that θ approaches π according to Fig. 2(b). Our MD simulations confirm that the deformation is reversible in the strain interval from -78 to 68%, implying excellent mechanical resilience. A quasistatic simulation [52] is conducted for compression of GMS 1 by a strain of -7.5% followed by equilibration for 1 ns with fixed length in the x direction and the stress component

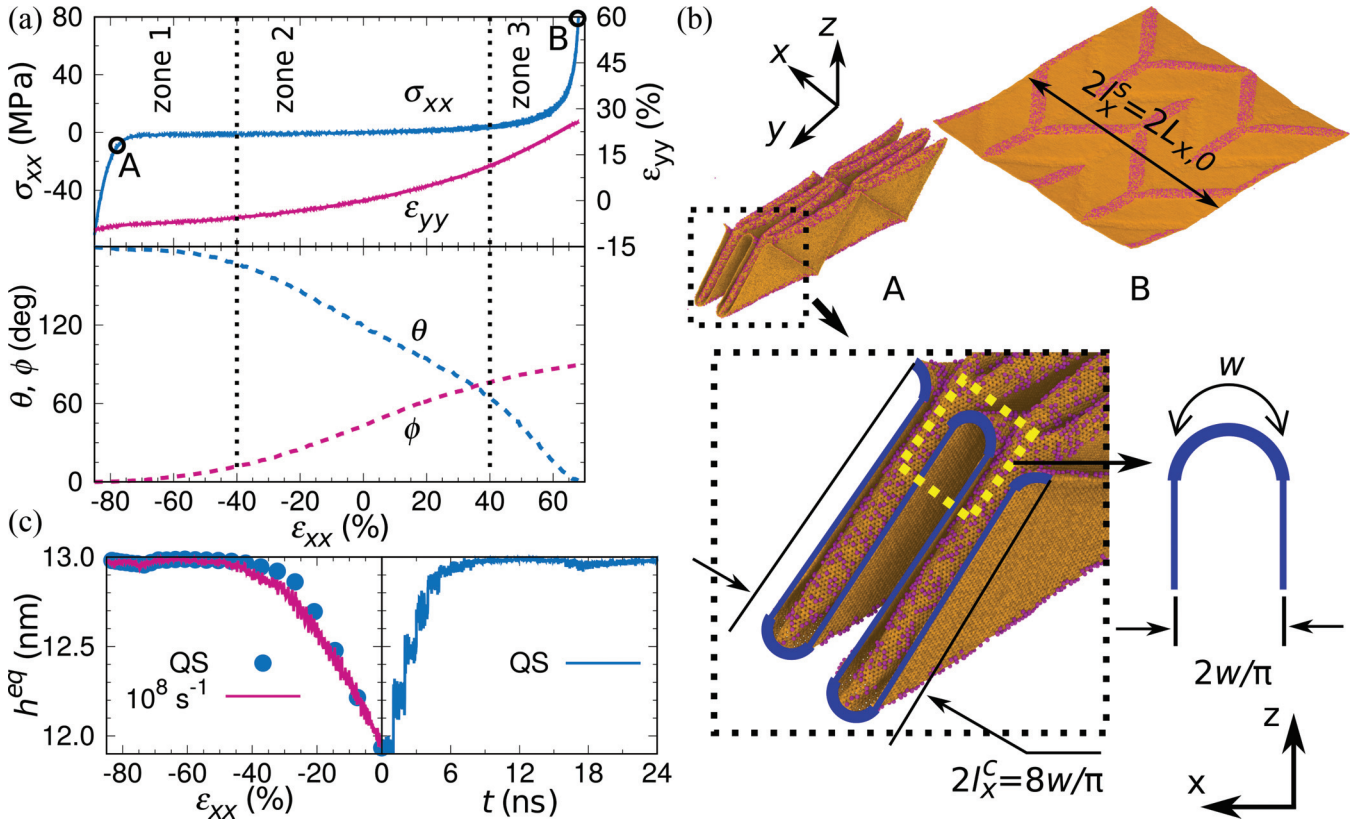

FIG. 2. Mechanical response of GMS 1 under uniaxial stress in the x direction at 300 K: (a) σ_{xx}, ϵ_{yy}, θ, and ϕ as functions of ϵ_{xx}. (b) Structure at points A and B marked in (a). (c) h^{eq} as a function of ϵ_{xx} for a strain rate of 10^8 s^{-1} and a quasistatic simulation (QS; the dependence on the simulation time is shown).

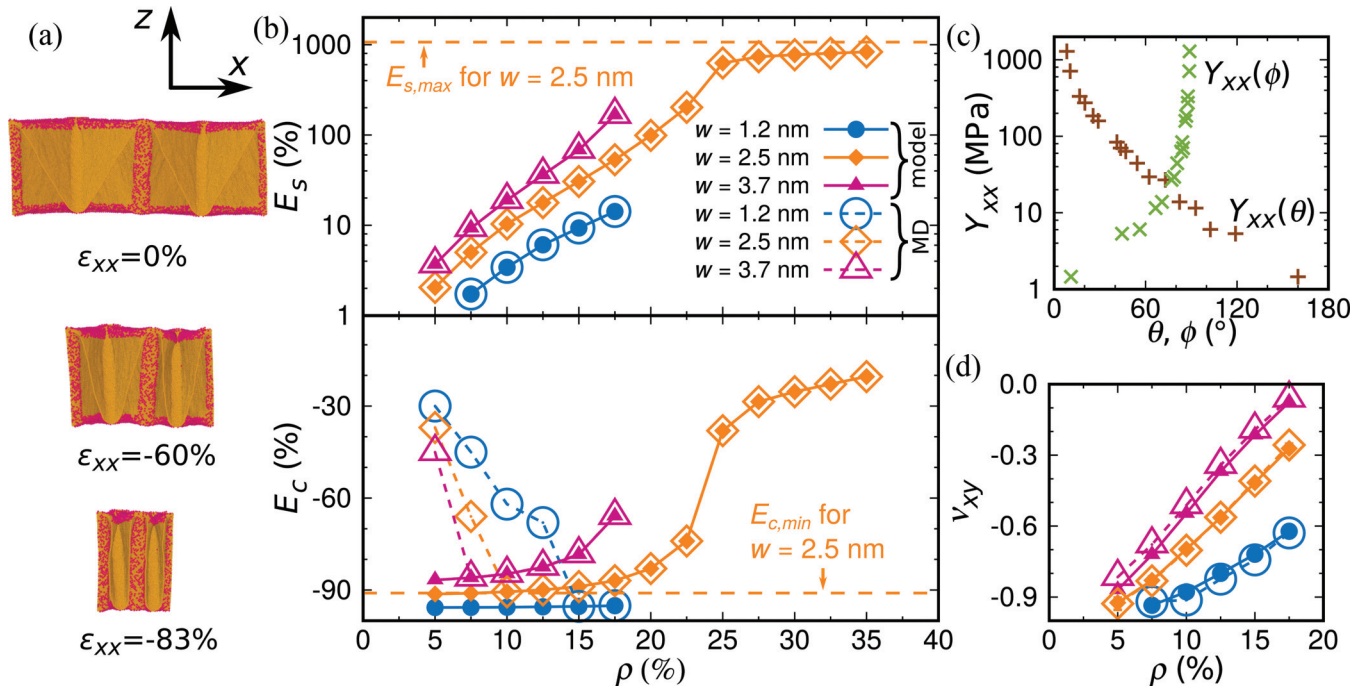

FIG. 3. GMSs with $L_{x,0} = L_{y,0} = 36.7$ nm: (a) deformation without buckling for $\rho = 20\%$, (b) effect of w and ρ on E_s and E_c, (c) Y_{xx} as a function of θ and ϕ, and (d) effect of w and ρ on ν_{xy}. The legend of (b) applies also to (d).

in the y direction controlled to be zero to stabilize the total energy (NPT ensemble). This process is repeated until the strain reaches -0.85%. The results in Fig. 2(c) indicate negligible effects of the strain rate (agreement between the strain rate of 10^8 s^{-1} and the quasistatic simulation) and that the folds do not reverse during the compression.

Figure 2(a) also presents ϵ_{yy} as a function of ϵ_{xx}, showing that GMS 1 expands/shrinks in the y direction when the structure is stretched/compressed (auxeticity). Poisson's ratio of GMS 1, calculated as the negative slope of $\epsilon_{yy}(\epsilon_{xx})$ in the strain interval from -1 to 1%, turns out to be -0.20, whereas that of pristine graphene (strain interval from 0 to 2%) turns out to be 0.24. More importantly, we find robust auxeticity in the whole considered range of applied strain.

While we have seen that GMS 1 exhibits high flexibility (under both tension and compression) and auxeticity, in contrast to pristine graphene, we now show that these properties can be effectively tuned by controlling the geometry of the GMS. We define the stretchability

$$E_s = \frac{l_x^s}{l_x^{\rm eq}} - 1 \sim \frac{L_{x,0}}{l_x^{\rm eq}} - 1, \tag{2}$$

and the compressibility

$$E_c = \frac{l_x^c}{l_x^{\rm eq}} - 1 \sim \frac{4w}{\pi l_x^{\rm eq}} - 1, \tag{3}$$

where $l_x^{\rm eq}$, l_x^s, and l_x^c are the lengths of the unit cell in the x direction in the equilibrium state, in the state $\theta = 0$, and in the state $\theta = \pi$, respectively, and we have approximated $l_x^s = L_{x,0}$ and $l_x^c = 4w/\pi$ [see Fig. 2(b)]. Equations (2) and (3) imply that E_s and E_c can be tuned by $l_x^{\rm eq}$. For $w \ll L_{x,0}$ we have ($\theta \in [0, \pi]$)

$$l_x^{\rm eq} = L_{x,0}\sqrt{\frac{1+\cos\theta}{2}}. \tag{4}$$

Since already for a single fold $\theta \propto w\rho$ [53], E_s and E_c increase for increasing w and ρ.

Quantitative calculation of E_s using Eq. (2) and E_c using Eq. (3) requires $l_x^{\rm eq}$, which we obtain as the average from a 500-ps MD simulation of the equilibrium state. We determine the effect of ρ on E_s and E_c by considering GMSs with ρ in the range from 5.0 to 35.0% (common $L_{x,0} = L_{y,0} = 36.7$ nm and $w = 2.5$ nm). We find that E_s (from 2 to 843%) and E_c (from -96 to -19%) increase strongly in this range of ρ, indicating high tunability. The upper limit of E_s is $E_{s,\max} = (\frac{\pi}{4}\frac{L_{x,0}}{w} - 1)$ for $l_x^{\rm eq} = l_x^c = 4w/\pi$ [Fig. 2(b)] and the lower limit of E_c is $E_{c,\min} = (\frac{4w}{\pi L_{x,0}} - 1)$ for $l_x^{\rm eq} = L_{x,0}$. In the case $L_{x,0} = L_{y,0} = 36.7$ nm and $w = 2.5$ nm we obtain $E_{s,\max} = 1068\%$ and $E_{c,\min} = -91\%$. We note that Eqs. (2) and (3) neglect possible failure during the loading, i.e., the actual stretchability/compressibility can be smaller than E_s/E_c. For this reason, we stretch/compress each GMS to its E_s/E_c using MD simulations with a strain rate of $\pm 10^8$ s^{-1}. If a GMS fails before reaching E_s/E_c, the failure strain is regarded as the stretchability/compressibility. We observe no failure under tension, whereas buckling occurs at $\rho = 5$ and 7.5%. At these values the model and MD results in Fig. 3(b) diverge, because the model does not included buckling. An example of a deformation without buckling at $\rho = 20\%$ is shown in Fig. 3(a).

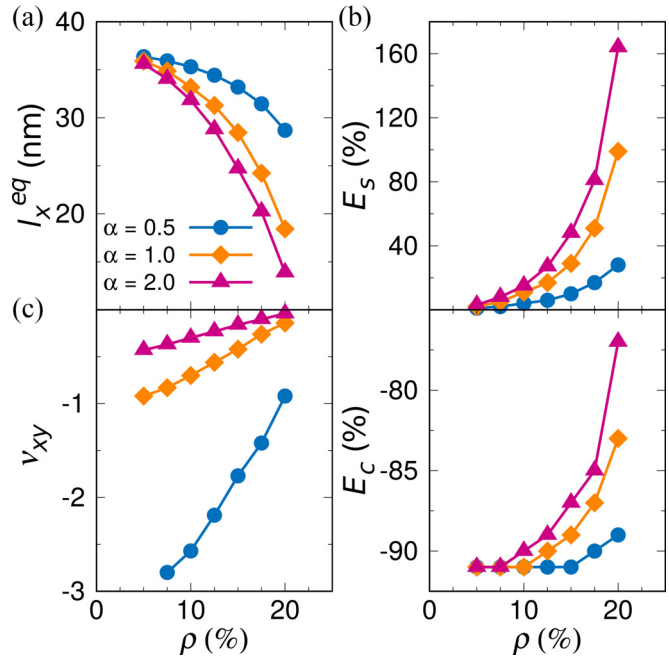

FIG. 4. Effect of α and ρ on (a) $l_x^{\rm eq}$, (b) E_s and E_c, and (c) ν_{xy}.

Turning to the effect of w on E_s and E_c, we consider GMSs with w in the range from 1.2 to 3.7 nm and ρ in the range from 5.0 to 17.5% (common $L_{x,0} = L_{y,0} = 36.7$ nm). We find that the effect of w is similar to that of ρ [Fig. 3(b)]. Furthermore, Y_{xx} falls in the range from 1.5 to 1287.7 MPa [Fig. 3(c)], which is about three orders of magnitude larger than reported for typical cellular graphene structures with similar E_c [54].

For the ideal Miura-origami structure (flapping without deformation and $w \ll L_{x,0}$) Poisson's ratio is given by [33]

$$\nu_{xy} = -\tan^2\phi/2. \tag{5}$$

As Fig. 1(c) implies $\theta = \arccos(2\frac{\sin^2(\phi/2)}{\sin^2\beta} - 1)$, we obtain

$$\nu_{xy} = -\left(\frac{\sin^2\beta(1+\cos\theta)}{2-\sin^2\beta(1+\cos\theta)}\right). \tag{6}$$

Figure 3(d) compares ν_{xy} obtained by Eq. (6), using θ from our MD simulations for the equilibrium state, with the MD results of the negative slope of $\epsilon_{xx}(\epsilon_{yy})$ for the GMSs of Fig. 3(a), both showing that ν_{xy} increases for increasing w and ρ. The fact that the two approaches provide closely related results indicates that the model behind Eq. (6) describes the fundamental physics very well. Minor differences are due to the fact that the GMSs deviate from the model assumptions of flapping without deformation and $w \ll L_{x,0}$.

Finally, we consider GMSs with $L_{x,0} = 36.7$ nm and $L_{y,0} = \alpha L_{x,0}$ for $\alpha = 0.5$, 1.0, and 2.0; $w = 2.5$ nm; and ρ in the range from 5.0 to 20.0%. The results of our MD simulations in Fig. 4(a) show that $l_x^{\rm eq}$ not only decreases with ρ, as expected, but also decreases significantly with α. This finding is due to the fact that θ depends not only on w and ρ but also on α

due to geometrical constraints (more restrictive for smaller α). Figure 4(b) shows that E_s and E_c increase with α, i.e., α is an additional effective parameter (besides w and ρ) to tune the flexibility of a GMS, especially the stretchability. Furthermore, as α affects ν_{xy} via both β and θ [Eq. (6)], ν_{xy} also can be effectively tuned, e.g., for our GMSs from -2.89 to -0.01 [Fig. 4(c)], which is a much wider range than reported for any auxetic graphene-based structure.

IV. CONCLUSIONS

In conclusion, MD simulations demonstrate high tunability of the flexibility and negative Poisson's ratio of GMSs formed by pattern-based hydrogenation of graphene sheets (by means of the parameters w, ρ, and α), providing an approach to control the material properties through three-dimensional geometry. Our results show that such GMSs also can exhibit superflexibility and that the auxeticity can be maintained even under large tensile and compressive strains. It turns out that the origami approach provides the unprecedented property of simultaneous superflexibility and auxeticity. The proposed GMSs thus have great potential in applications requiring superflexibility and/or auxeticity. For example, they can improve the performance of high sensitivity strain sensors [20].

ACKNOWLEDGMENTS

The research reported in this publication was supported by funding from King Abdullah University of Science and Technology (KAUST). This work used computational resources of the Supercomputing Laboratory at KAUST. S.Y.K. acknowledges support from the Mid-Career Researcher Support Program (No. 2019R1A2C2011312) of the National Research Foundation (NRF) of Korea.

[1] T. Das, B. K. Sharma, A. K. Katiyar, and J.-H. Ahn, Graphene-based flexible and wearable electronics, J. Semicond. **39**, 011007 (2018).

[2] K. Chen, Q. Wang, Z. Niu, and J. Chen, Graphene-based materials for flexible energy storage devices, J. Energy Chem. **27**, 12 (2018).

[3] Y. Zhang, Q. Wan, and N. Yang, Recent advances of porous graphene: Synthesis, functionalization, and electrochemical applications, Small **15**, 1903780 (2019).

[4] H. Hu, Z. Zhao, W. Wan, Y. Gogotsi, and J. Qiu, Ultralight and highly compressible graphene aerogels, Adv. Mater. **25**, 2219 (2013).

[5] H. Bi, I.-W. Chen, T. Lin, and F. Huang, A new tubular graphene form of a tetrahedrally connected cellular structure, Adv. Mater. **27**, 5943 (2015).

[6] Y. Wu, N. Yi, L. Huang, T. Zhang, S. Fang, H. Chang, N. Li, J. Oh, J. A. Lee, M. Kozlov, A. C. Chipara, H. Terrones, P. Xiao, G. Long, Y. Huang, F. Zhang, L. Zhang, X. Lepró, C. Haines, M. D. Lima, N. P. Lopez, L. P. Rajukumar, A. L. Elias, S. Feng, S. J. Kim, N. T. Narayanan, P. M. Ajayan, M. Terrones, A. Aliev, P. Chu, Z. Zhang, R. H. Baughman, and Y. Chen, Three-dimensionally bonded spongy graphene material with super compressive elasticity and near-zero Poisson's ratio, Nat. Commun. **6**, 6141 (2015).

[7] H.-L. Gao, Y.-B. Zhu, L.-B. Mao, F.-C. Wang, X.-S. Luo, Y.-Y. Liu, Y. Lu, Z. Pan, J. Ge, W. Shen, Y.-R. Zheng, L. Xu, L.-J. Wang, W.-H. Xu, H.-A. Wu, and S.-H. Yu, Super-elastic and fatigue resistant carbon material with lamellar multi-arch microstructure, Nat. Commun. **7**, 12920 (2016).

[8] C. Wang, C. Zhang, and S. Chen, The microscopic deformation mechanism of 3D graphene foam materials under uniaxial compression, Carbon **109**, 666 (2016).

[9] H. Kashani, Y. Ito, J. Han, P. Liu, and M. Chen, Extraordinary tensile strength and ductility of scalable nanoporous graphene, Sci. Adv. **5**, eaat6951 (2019).

[10] L. Lu, J. T. M. De Hosson, and Y. Pei, Three-dimensional micron-porous graphene foams for lightweight current collectors of lithium-sulfur batteries, Carbon **144**, 713 (2019).

[11] L. Qiu, B. Huang, Z. He, Y. Wang, Z. Tian, J. Z. Liu, K. Wang, J. Song, T. R. Gengenbach, and D. Li, Extremely low density and super-compressible graphene cellular materials, Adv. Mater. **29**, 1701553 (2017).

[12] Z. Qi, D. K. Campbell, and H. S. Park, Atomistic simulations of tension-induced large deformation and stretchability in graphene kirigami, Phys. Rev. B **90**, 245437 (2014).

[13] A. R. Ruyack, A. W. Barnard, B. Kobrin, D. A. Muller, J. W. Kevek, K. L. McGill, M. K. Blees, P. L. McEuen, P. A. Rose, P. Y. Huang, and S. P. Roberts, Graphene kirigami, Nature (London) **524**, 204 (2015).

[14] P. Z. Hanakata, E. D. Cubuk, D. K. Campbell, and H. S. Park, Accelerated Search and Design of Stretchable Graphene Kirigami Using Machine Learning, Phys. Rev. Lett. **121**, 255304 (2018).

[15] M. A. Dias, M. P. McCarron, D. Rayneau-Kirkhope, P. Z. Hanakata, D. K. Campbell, H. S. Park, and D. P. Holmes, Kirigami actuators, Soft Matter **13**, 9087 (2017).

[16] W. Yang, Z.-M. Li, W. Shi, B.-H. Xie, and M.-B. Yang, Review on auxetic materials, J. Mater. Sci. **39**, 3269 (2004).

[17] S. Jacobs, C. Coconnier, D. DiMaio, F. Scarpa, M. Toso, and J. Martinez, Deployable auxetic shape memory alloy cellular antenna demonstrator: Design, manufacturing and modal testing, Smart Mater. Struct. **21**, 075013 (2012).

[18] H. Cao, A. Zulifqar, T. Hua, and H. Hu, Bi-stretch auxetic woven fabrics based on foldable geometry, Text. Res. J. **89**, 2694 (2019).

[19] K.-I. Jang, H. U. Chung, S. Xu, C. H. Lee, H. Luan, J. Jeong, H. Cheng, G.-T. Kim, S. Y. Han, J. W. Lee, J. Kim, M. Cho, F. Miao, Y. Yang, H. N. Jung, M. Flavin, H. Liu, G. W. Kong, K. J. Yu, S. I. Rhee, J. Chung, B. Kim, J. W. Kwak, M. H. Yun, J. Y. Kim, Y. M. Song, U. Paik, Y. Zhang, Y. Huang, and J. A. Rogers, Soft network composite materials with deterministic and bio-inspired designs, Nat. Commun. **6**, 6566 (2015).

[20] Y. Jiang, Z. Liu, N. Matsuhisa, D. Qi, W. R. Leow, H. Yang, J. Yu, G. Chen, Y. Liu, C. Wan, Z. Liu, and X. Chen, Auxetic mechanical metamaterials to enhance sensitivity of stretchable strain sensors, Adv. Mater. **30**, 1706589 (2018).

[21] R. Lakes, Foam structures with a negative Poisson's ratio, Science **235**, 1038 (1987).

[22] K. W. Wojciechowski, Constant thermodynamic tension Monte Carlo studies of elastic properties of a two-dimensional system of hard cyclic hexamers, Mol. Phys. **61**, 1247 (1987).

[23] K. W. Wojciechowski, F. Scarpa, J. N. Grima, and A. Alderson, Auxetics and other systems of anomalous characteristics, Phys. Status Solidi B **256**, 1800736 (2019).

[24] D. T. Ho, S.-D. Park, S.-Y. Kwon, K. Park, and S. Y. Kim, Negative Poisson's ratios in metal nanoplates, Nat. Commun. **5**, 3255 (2014).

[25] C. Huang and L. Chen, Negative Poisson's ratio in modern functional materials, Adv. Mater. **28**, 8079 (2016).

[26] A. Rafsanjani and D. Pasini, Bistable auxetic mechanical metamaterials inspired by ancient geometric motifs, Extreme Mech. Lett. **9**, 291 (2016).

[27] T.-C. Lim, Analogies across auxetic models based on deformation mechanism, Phys. Status Solidi RRL **11**, 1600440 (2017).

[28] V. H. Ho, D. T. Ho, S.-Y. Kwon, and S. Y. Kim, Negative Poisson's ratio in periodic porous graphene structures, Phys. Status Solidi B **253**, 1303 (2016).

[29] J.-W. Jiang and H. S. Park, Negative Poisson's ratio in single-layer graphene ribbons, Nano Lett. **16**, 2657 (2016).

[30] K. V. Zakharchenko, M. I. Katsnelson, and A. Fasolino, Finite Temperature Lattice Properties of Graphene Beyond the Quasiharmonic Approximation, Phys. Rev. Lett. **102**, 046808 (2009).

[31] J. N. Grima, S. Winczewski, L. Mizzi, M. C. Grech, R. Cauchi, R. Gatt, D. Attard, K. W. Wojciechowski, and J. Rybicki, Tailoring graphene to achieve negative Poisson's ratio properties, Adv. Mater. **27**, 1455 (2015).

[32] H. Qin, Y. Sun, J. Z. Liu, M. Li, and Y. Liu, Negative Poisson's ratio in rippled graphene, Nanoscale **9**, 4135 (2017).

[33] M. Schenk and S. D. Guest, Geometry of Miura-folded metamaterials, Proc. Natl. Acad. Sci. USA **110**, 3276 (2013).

[34] C. Lv, D. Krishnaraju, G. Konjevod, H. Yu, and H. Jiang, Origami based mechanical metamaterials, Sci. Rep. **4**, 5979 (2014).

[35] B. G. Chen, B. Liu, A. A. Evans, J. Paulose, I. Cohen, V. Vitelli, and C. D. Santangelo, Topological Mechanics of Origami and Kirigami, Phys. Rev. Lett. **116**, 135501 (2016).

[36] D. W. Brenner, O. A. Shenderova, J. A. Harrison, S. J. Stuart, B. Ni, and S. B. Sinnott, A second-generation reactive empirical bond order (REBO) potential energy expression for hydrocarbons, J. Phys.: Condens. Matter **14**, 783 (2002).

[37] G. J. Martyna, D. J. Tobias, and M. L. Klein, Constant pressure molecular dynamics algorithms, J. Chem. Phys. **101**, 4177 (1994).

[38] W. Shinoda, M. Shiga, and M. Mikami, Rapid estimation of elastic constants by molecular dynamics simulation under constant stress, Phys. Rev. B **69**, 134103 (2004).

[39] S. Plimpton, Fast parallel algorithms for short-range molecular dynamics, J. Comput. Phys. **117**, 1 (1995).

[40] A. Stukowski, Visualization and analysis of atomistic simulation data with OVITO—the open visualization tool, Modell. Simul. Mater. Sci. Eng. **18**, 015012 (2010).

[41] Q. Lu, M. Arroyo, and R. Huang, Elastic bending modulus of monolayer graphene, J. Phys. D **42**, 102002 (2009).

[42] R. Nicklow, N. Wakabayashi, and H. G. Smith, Lattice dynamics of pyrolytic graphite, Phys. Rev. B **5**, 4951 (1972).

[43] K. E. Whitener, Jr., Review article: Hydrogenated graphene: A users guide, J. Vac. Sci. Technol. A **36**, 05G401 (2018).

[44] M. K. Rehmann, Y. B. Kalyoncu, M. Kisiel, N. Pascher, F. J. Giessibl, F. Müller, K. Watanabe, T. Taniguchi, E. Meyer, M.-H. Liu, and D. M. Zumbühl, Characterization of hydrogen plasma defined graphene edges, Carbon **150**, 417 (2019).

[45] D. C. Elias, R. R. Nair, T. M. G. Mohiuddin, S. V. Morozov, P. Blake, M. P. Halsall, A. C. Ferrari, D. W. Boukhvalov, M. I. Katsnelson, A. K. Geim, and K. S. Novoselov, Control of graphene's properties by reversible hydrogenation: Evidence for graphane, Science **323**, 610 (2009).

[46] R. Balog, B. Jørgensen, J. Wells, E. Lægsgaard, P. Hofmann, F. Besenbacher, and L. Hornekær, Atomic hydrogen adsorbate structures on graphene, J. Am. Chem. Soc. **131**, 8744 (2009).

[47] X. Zhang, Y. Huang, S. Chen, N. Y. Kim, W. Kim, D. Schilter, M. Biswal, B. Li, Z. Lee, S. Ryu, C. W. Bielawski, W. S. Bacsa, and R. S. Ruoff, Birch-type hydrogenation of few-layer graphenes: Products and mechanistic implications, J. Am. Chem. Soc. **138**, 14980 (2016).

[48] J. Liu, S. Chen, R. Papadakis, and H. Li, Nanoresolution patterning of hydrogenated graphene by electron beam induced CH dissociation, Nanotechnology **29**, 415304 (2018).

[49] I.-S. Byun, D. Yoon, J. S. Choi, I. Hwang, D. H. Lee, M. J. Lee, T. Kawai, Y.-W. Son, Q. Jia, H. Cheong, and B. H. Park, Nanoscale lithography on monolayer graphene using hydrogenation and oxidation, ACS Nano **5**, 6417 (2011).

[50] X. Wang, G. Zhang, Z. Wang, L. Yang, X. Li, J. Jiang, and Y. Luo, Metal-enhanced hydrogenation of graphene with atomic pattern, Carbon **143**, 700 (2019).

[51] D. M. Heyes, Pressure tensor of partial-charge and point-dipole lattices with bulk and surface geometries, Phys. Rev. B **49**, 755 (1994).

[52] N. Vu-Bac, P. M. A. Areias, and T. Rabczuk, A multiscale multisurface constitutive model for the thermo-plastic behavior of polyethylene, Polymer **105**, 327 (2016).

[53] D. T. Ho, V. H. Ho, V. Babar, S. Y. Kim, and U. Schwingenschlögl, Complex three-dimensional graphene structures driven by surface functionalization, Nanoscale **12**, 10172 (2020).

[54] N. Ni, S. Barg, E. Garcia-Tunon, F. Macul Perez, M. Miranda, C. Lu, C. Mattevi, and E. Saiz, Understanding mechanical response of elastomeric graphene networks, Sci. Rep. **5**, 13712 (2015).